# Experimental study on pin-fin shapes for bubble growth and heat transfer in microchannel heat exchangers

Zhaohua Li [a,1], Xiucong Zhao [a,1], Yongfa Qin [a], Xiang Wang [b,*]

[a] School of Mechanical Engineering, Yangzhou University, Yangzhou, 225012, China
[b] College of Engineering Design and Physical Sciences, Brunel University of London, Uxbridge, UB8 3PH, UK

GRAPHICAL ABSTRACT
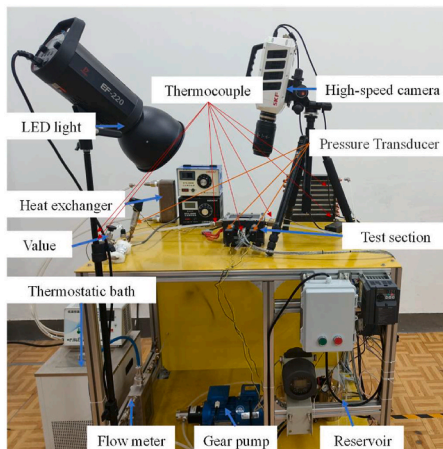
ARTICLE INFO

ABSTRACT

The microchannel heat exchangers (MCHXs) with pin-fin array using electronic fluoride liquid have become one of the promising solutions for dissipating excessive localised heat flux due to the continuous advancement in computing capabilities and the miniaturization of electronic devices. However, the detailed mechanisms by which pin-fin shape influences microscale flow patterns and thermal behaviour remain insufficiently understood, necessitating further in-depth investigation. This study experimentally evaluates the performance of the MCHXs with circular,

* Corresponding author.
  E-mail address: Xiang.Wang@brunel.ac.uk (X. Wang).
[1] Zhaohua Li and Xiucong Zhao contributed equally to this manuscript.

diamond, and drop pin-fins. A high-speed camera is used to visualise the bubble growth process and investigate the flow regimes variation under different heat fluxes and flow rates. The results show that, at a heat flux of 90 kW/m^2, the maximum equivalent bubble diameters for diamond, circular, and drop are 4.6 mm, 4.1 mm and 3.9 mm, respectively, leading to the lowest pressure drop for the MCHX with drop shapes.

1. Introduction

As high-power electronic devices advance toward greater miniaturization and integration, their heat flux has escalated over 300 W/cm^2, surpassing the heat dissipation capacity of conventional cooling technologies [1–3]. In contrast, microchannel heat transfer technology, known for its high efficiency and compact structure, has emerged as a promising solution for next-generation thermal management [4].

The instability of phase-change heat transfer in micro-channel heat exchanger (MCHS) has been a major bottleneck in the development of microscale cooling technologies, as various parameters, including inlet velocity, heat flux, channel diameter, and vapor quality, significantly influence the transition mechanisms of two-phase flow regimes [5–9]. Gu et al. [10] experimentally investigated flow regime development in a steam-heated vertical rectangular narrow channel, identifying five primary two-phase flow patterns: bubble flow, confined bubble flow, slug flow, churn flow, and annular flow. As mass flow increases, churn and annular flow fractions gradually increase at low vapor quality. Yu et al. [11] studied the effect of sudden heat flux increments on two-phase flow regimes in flow boiling, revealing that different heat flux increase rates lead to distinct flow regime transitions. A sudden heat flux rise induces severe flow regime fluctuations, particularly in bubble flow, which rapidly evolves into annular flow and may even cause localized dry out. Feng et al. [6] carried out experimental research on flow boiling heat transfer and flow regimes of R245fa in a smooth horizontal MCHX. The results identified bubble/slug flow, liquid film evaporation, and annular flow as dominant two-phase flow regimes. Among them, annular flow exhibited superior heat transfer capacity, though the study did not analyse the impact of flow regimes on pressure drop. Xue et al. [12] investigated the flow behaviour of azeotropic R290/R600a mixture within a 6 mm horizontal MCHX, showing that at high heat flux, slug flow rarely occurs. Increasing heat flux accelerates the boiling process, leading to a significant increase in local vapor velocity. Chang et al. [13] performed three-dimensional unsteady numerical simulations on the environmentally friendly refrigerant R1234ze(E) in a small tube. Their results demonstrated that with increasing vapor quality. Additionally, higher mass flow leads to a reduction in the vapor quality required for flow regime transitions. Shin et al. [14] investigated the flow regime evolution of oil-gas mixtures in horizontal tubes, identifying seven distinct flow patterns: smooth stratified flow, wavy stratified flow, annular flow, plug flow, slug flow, bubble flow, and dispersed bubble flow. Rong et al. [15] examined vertical annular channels with different gap sizes, concluding that higher heat flux, fluid velocity, and subcooling shorten bubble growth cycles, while bubble growth rates depend on the distance between the bubble and the heated wall. Although these studies have explored the effects of various parameters on the two-phase flow state and heat transfer efficiency, they are limited to room temperature refrigerants, and research on refrigerants such as electronic fluorinated liquids is very limited.

During flow boiling, the interfacial morphology is influenced by fluid velocity, microstructure surface characteristics, and fluid physical properties, leading to various flow regimes. Extensive research has been conducted on structural optimization [16,17], surface roughness [18,19], and porosity [20,21] to improve flow behaviour at the heat transfer interface and enhance MCHX heat transfer capability. Some studies specifically investigated the impact of pin-fin shape on heat transfer enhancement in MCHXs. Pin-fin structure is one of the most efficient methods to improve the heat transfer capability of MCHX. Numbers of studies have been conducted to investigate the impact of pin-fin shape on heat transfer enhancement in MCHXs. Darekar et al. [22] experimentally studied two-phase flow regimes in Y-junction MCHXs. Their findings indicated that as the diameter of MCHX increases, flow regime transitions occur at lower flow velocities. Donaldson et al. [23] investigated the mechanism of two-phase flow regime transitions in serpentine MCHXs with different curvature radii, revealing that smaller curvature radio promote bubble breakup and enhance heat transfer. Moharana et al. [24] performed numerical simulations on bubble formation and surface movement in circular, elliptical, and combined circular-elliptical tube bundles. Their results demonstrated that elliptical tube bundles increase heat transfer by 3 %–26 % while reducing pressure drop by 56 %–94 %. Odumosu et al. [25] used numerical simulations to analyse flow boiling heat transfer and bubble growth in wavy MCHXs with different corrugation levels. They found that as MCHX corrugation increases, bubble generation intensifies, and bubble-induced disturbances enhance heat transfer. Peng et al. [26] conducted 3D CFD simulations of flow and heat transfer in multi-jet MCHXs, showing that multi-jet MCHXs outperform conventional MCHXs in both heat transfer and pressure drop characteristics.

In summary, extensive research has explored flow boiling characteristics and heat transfer optimization in MCHXs with different shapes. However, the studies for the influence of microchannel pin-fin structures on flow regime transitions and heat transfer mechanisms remain limited. To address this gap, the present study systematically examines three distinct pin-fin shapes (circular, diamond, and drop) to analyse their effects on internal microscopic flow, heat transfer, and pressure characteristics within MCHXs. The bubble growth process was visualized by using high-speed camera, and the evolution of flow regimes with increasing heat flux was characterized by the three pin-fin shapes. The findings provide a theoretical foundation for enhancing the heat transfer performance of MCHXs for electrical cooling.

2. Experimental systems and data processing

2.1. Experimental test rig

A two-phase flow microchannel heat sink test rig was constructed as shown in Fig. 1 to investigate the effects of different pin-fin shapes on the two-phase flow and heat transfer characteristics in MCHXs. The test rig includes MCHX testing module, flow control module, cooling module, temperature and pressure acquisition module, and high-speed image acquisition module.

The structure of the MCHX testing module is shown in detail in Fig. 2. From top to bottom, the upper sealing cover contains a visualization window for capturing two-phase flow images. The MCHX is positioned beneath this cover, and its surface is machined into fins of different shapes. The coolant inlet and outlet are arranged on both sides, where two pressure sensors are installed to monitor the pressure drop. Nine temperature sensors are arranged in a 3×3 layout on the copper surface to evaluate the heat transfer characteristics. Adjacent to the MCHX is the heating module, consisting of eight cartridge heaters embedded in copper blocks and powered by an adjustable DC power supply with a maximum capacity of 700 W. In the experiments, the heating power applied to the MCHX was controlled within 20–140 W, corresponding to average heat fluxes of 3.9–27.3 W/cm^2. During operation, the mass flow rate of Novec-649 was varied between 0.6 and 1.4 g/s, and the inlet liquid temperature was maintained at $22 \pm 0.3\,^\circ$C to ensure consistent and repeatable testing conditions. The entire assembly is sealed with O-rings and vacuum sealant to maintain airtightness, and insulation material is applied externally to minimise heat loss.

Fig. 3 shows the pin-fin shapes and arrangement structure of the processed MCHX. As shown in the figure, three shapes of pin-fin arrays including circular, drop, and diamond, are processed on the surface of a 50 * 50 mm copper block. The circular, diamond, and teardrop pin-fin configurations were designed with the same total channel volume and pin-fin arrangement density, ensuring identical fluid volume for all cases. Only the pin-fin cross-sectional shape varies among the three structures, enabling a direct comparison of their heat transfer and flow performance.

Novec-649 is used as a coolant, and its thermophysical properties are listed in Table 1.

In this work, experiments were conducted on the two-phase flow and heat transfer capacity in microchannel heat sinks under different pin-fin shapes, flow rates, and heating powers. Before the experiment, open the pump and valve to circulate the coolant and exhaust the gas inside the microchannel heat sinks, in order to reduce the impact of residual air in the system on the results. Then adjust the output power of the adjustable DC power supply and record the data after the two-phase manifold and temperature are stabilized. The experimental data was collected in real-time through temperature sensors, pressure sensors, and high-speed cameras.

2.2. Data analysis

The flow velocity of the coolant at the MCHX inlet is specified as

$$v_{in} = \frac{\dot{m}}{\rho A_{in}} \tag{1}$$

where ρ is the liquid density, A_{in} represents the cross-sectional area at the MCHX inlet, and $\dot{m}$ is the mass flow rate.

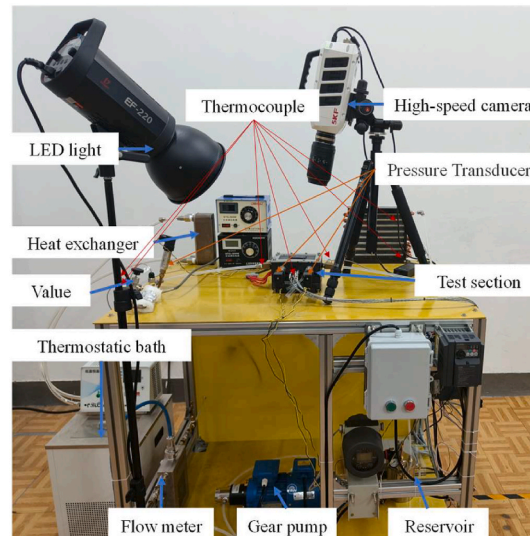Hence, the mean velocity within the MCHX can be represented by

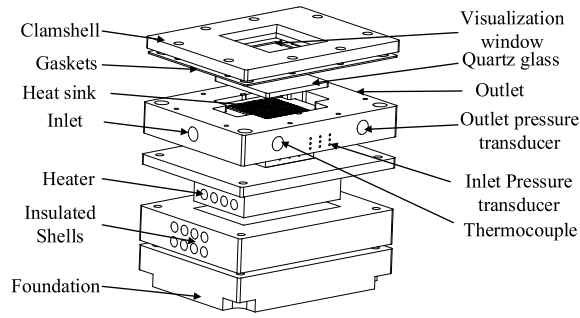**Fig. 1.** The configuration and instrumentation for two-phase flow microchannel experiments.

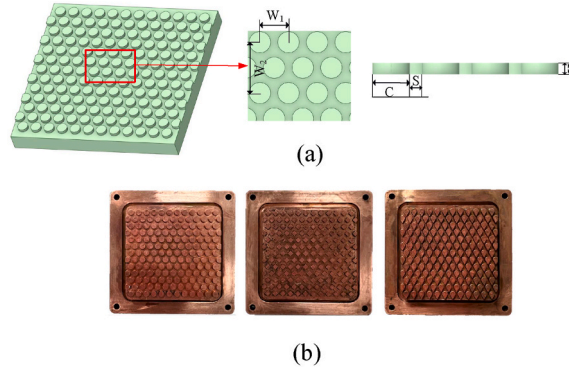**Fig. 2.** The schematic diagrams of MCHX testing module.

Fig. 3. The structural and physical diagrams of MCHX.

Table 1
Thermophysical properties of Novec-649.

Property	Value	Property	Value
Molecular weight	316.04 g/mol	Boiling point	49 °C
Liquid density	1630 kg/m³	Vapor density	8.6 kg/m³
Dynamic viscosity	0.61 mPa s	Surface tension	11.9 mN/m
Specific heat	1100 J/(kg·K)	Thermal conductivity	0.057 W/(m·K)

$$v = \left(\frac{W_1 W_2 - \frac{\pi D^2}{4}}{W_1 W_2} \right) v_{in} \qquad (2)$$

where W1 and W2 respectively denote the longitudinal and lateral distances separating the centers of two fins.

Hence, the Renold number (Re) is determined by

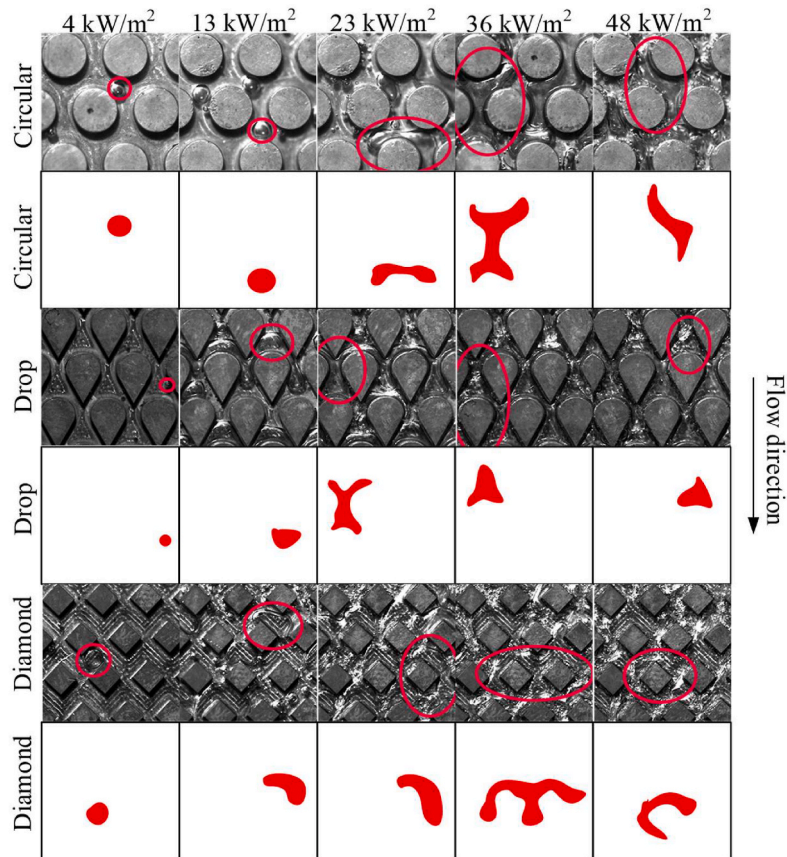$$Re = \frac{\rho v D_h}{\mu} \qquad (3)$$

where ρ is the liquid density, μ is the liquid kinematic viscosity, and D_h is the hydraulic diameter.
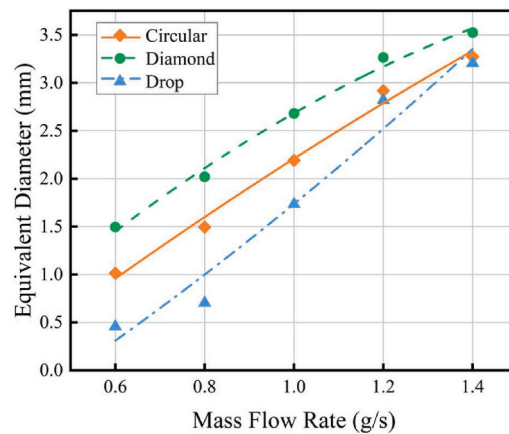
The hydraulic diameter D_h is defined as

$$D_h = \frac{4 V_{flow}}{A_{HT}} \qquad (4)$$

in which

$$V_{flow} = \left(W_1 W_2 - \frac{\pi D^2}{4} \right) H_{pin} \qquad (5)$$

(a) Visualization of two-phase flow in MCHXs

(b) Variation of maximum equivalent bubble diameter under various mass flow rates

Fig. 4. Variation of the maximum equivalent bubble diameter for the MCHX under various mass flow rates and pin-fin shapes.

$$A_{HT} = (W_1 W_2) - \frac{\pi d^2}{4} + \pi D H_{pin} \tag{6}$$

Hence, the average heat flux, denoted by q, can be represented as

$$q = \frac{Q}{A} \tag{7}$$

where A is the area of the MCHX.

The experimental pressure drop is calculated as

$$\Delta P = P_{in} - P_{out} \tag{8}$$

where Pin is the pressure at the MCHX inlet and Pout is the pressure at the MCHX outlet.

The maximum equivalent bubble diameter $D_{b,max}$ was calculated as:

$$D_{b,max} = \frac{1}{N} \sum_{i=1}^{N} \left(\max_{j} D_{b,ij} \right) \tag{9}$$

where N is the total number of sampled frames, and $D_{b,ij}$ represents the equivalent diameter of the jth bubble detected in the ith frame.

The bubble identification and segmentation were performed using an image-processing algorithm adapted from the work of Wang [11]. This approach has been validated for accurate bubble detection and dynamic tracking.

2.3. Uncertainty analysis

All measurements were conducted using calibrated sensors and instruments. The overall uncertainties of the measured and derived parameters were estimated according to the standard propagation-of-error method. The maximum uncertainties were ±0.5 K for temperature, ±0.25 % FS for pressure, ±0.2 % FS for flow rate, and ±0.1 mm for bubble diameter obtained from image calibration.

For a quantity R calculated as a function of independent variables $x_1, x_2, \ldots, x_n$, the combined uncertainty U_R can be expressed as:

$$U_R = \sqrt{\sum_{i=1}^{n} \left(\frac{\partial R}{\partial x_i} U_{x_i} \right)^2} \tag{10}$$

where U_{x_i} denotes the uncertainty of variable x_i.

The uncertainty in the calculated heat flux was estimated to be ±3.5 %, and that of the Reynolds number was ±2.3 %. The uncertainty in heat flux primarily arises from the measurement accuracy of the heating power and the effective heat transfer area, whereas the uncertainty in the Reynolds number is mainly attributed to the uncertainties in mass flow rate, fluid properties, and hydraulic diameter. The steady-state condition was defined as a temperature fluctuation of less than 0.2 °C over a duration of 60 s. Before each experiment, the working fluid was degassed for 30 min under a vacuum of approximately −90 kPa to ensure consistent nucleation behaviour.
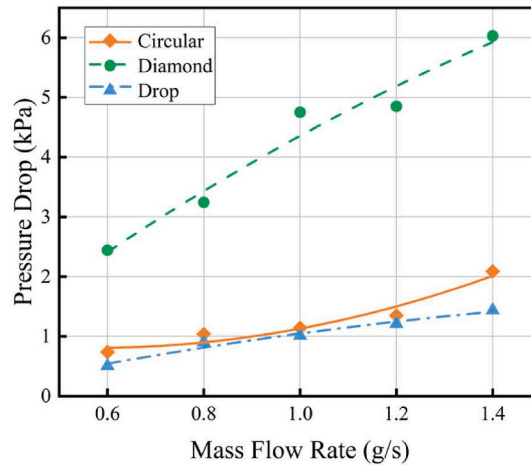

Fig. 5. Comparison of pressure drop in MCHXs with different pin-fin shapes under various flow rates.

3. Results and discussions

Fig. 4 (a) presents visualized two-phase flow and extracted bubbles of Novec-649 in MCHXs with circular, diamond, and drop pin-fin arrays. Fig. 4 (b) illustrates the effect of mass flow rate on the equivalent bubble diameter in MCHXs with different pin-fin shapes under heating powers ranging from 20 to 60 W, corresponding to specific heat fluxes. The findings suggest that in two-phase flow, the equivalent bubble diameter increases with increasing mass flow rates. This is mainly because the higher bubble number density at greater mass flow rates, which enhances bubble collision probability and facilitates the coalescence of smaller bubbles into larger ones. Additionally, MCHX shape has a considerable influence on bubble size, with the maximum bubble diameter following the order of drop, circular, and diamond. The maximum bubble diameters for diamond, circular, and drop are increased by 135 %, 292 %, and 601 %, respectively, with the mass flow rate increasing from 0.6 g/s to 1.4 g/s. In drop microchannels, the streamlined wall structure generates strong shear forces that stretch and break bubbles along the flow direction, resulting in smaller bubble size [27]. In contrast, circular microchannels exert a weaker stretching and fragmentation effect on bubbles, leading to a larger maximum bubble diameter compared to the drop shape. For diamond pin-fin array, bubbles tend to accumulate and coalesce in corner regions, leading to the largest maximum bubble diameter.

Fig. 5 presents a comparison of pressure drops in microchannels with different shapes under various flow rates. The results evidently show that the pressure drop rises with higher flow rates. When the cross-sectional area of the channel remains unchanged, increasing the flow rate causes the velocity of the fluid to rise. As a result, the frictional pressure drop correspondingly becomes more pronounced. When the mass flow rate rises from 0.6 g/s to 1.4 g/s, the pressure drops of the MCHX with circular, diamond, and waterdrop pin-fin shapes exhibit respective increases of 183 %, 147 %, and 184 %.

Fig. 6 presents a comparison of the maximum equivalent bubble diameter in MCHXs with different pin geometrics at a mass flow rate of 1.4 g/s with various heat fluxes. Overall, the diamond shape shows the highest equivalent diameter, while the maximum equivalent diameters for the rest two shapes are relatively the same. It is worth mentioning that as heat flux increases, the maximum equivalent diameters for all three shapes initially rise due to enhanced vapor generation, then decline as excessive nucleation induces violent bubble coalescence and fragmentation. This phenomenon is primarily attributed to enhanced heat transfer from the walls of MCHXs to the fluid, which intensifies local liquid superheating, making bubble formation and rapid growth more likely [28]. At a heat flux of 9 W/cm^2, the maximum equivalent bubble diameters for diamond, circular, and drop pin-fins are 4.6 mm, 4.1 mm and 3.9 mm, respectively.

Fig. 7 shows the variation of the pressure drops with heat fluxes for MCHXs with three pin-fin shapes at a mass flow rate of 1.4 g/s. The pressure drops across MCHXs with both three pin-fin shapes all increase with the heat flux. This phenomenon is primarily attributed to the morphological changes of large bubbles and their impact on flow resistance. As bubble size increases, bubbles can elongate and form slug flow, increasing the contact area with the channel walls, thereby enhancing flow resistance. Additionally, the interfacial tension effects of larger bubbles become more pronounced, further contributing to additional flow resistance [29]. However, the pressure drops reach the maximum heat power of 140 W while the corresponding equivalent diameters are decreased for three pin-fin shapes. This is because the progressive increase in heating power induces gradual bubble fragmentation, consistent with the trends documented in prior observations. The pressure drop follows the order of drop, circular, diamond microchannels, which is consistent with the earlier conclusions regarding maximum bubble diameter. At a heat power of 140 W, the diamond, circular, and drop pin-fin arrays have a pressure drop of 6.1 kPa, 2.1 kPa, and 1.4 kPa, respectively.

The bubble morphology in MCHXs significantly affects flow characteristics, heat transfer performance, mass transfer efficiency, and system stability, making its study essential. Fig. 8 illustrates the relationship between circularity and flow rate in MCHXs with different pin-fin shapes. Experimental results show that higher flow rates result in more deformed bubble shapes. Under low flow rate conditions, surface tension dominates, causing bubbles to remain spherical to maintain the minimum surface area for stability. As the flow rate increases, inertial forces strengthen, and shear forces intensify, leading to bubble deformation into ellipsoidal, flattened, or
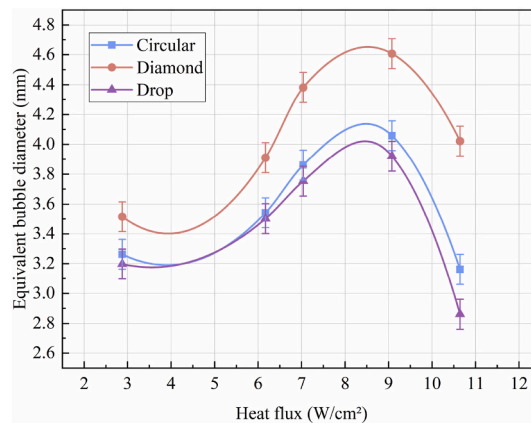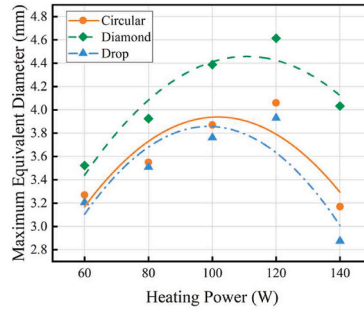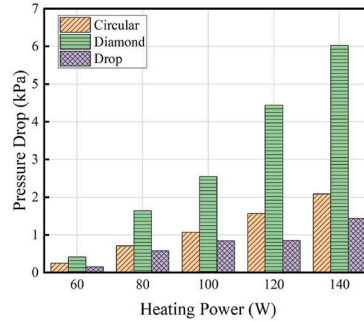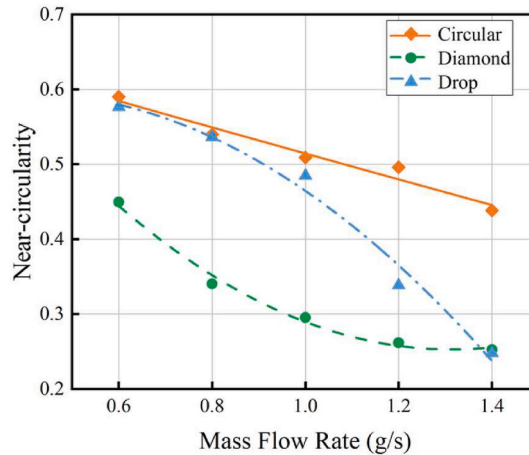

Fig. 6. Comparison of maximum equivalent bubble diameter in MCHXs with different shapes under various heat flux.

(a) Comparison of equivalent diameters under different heating powers

(b) Comparison of pressure drop under different heating powers

Fig. 7. Influence of pressure drop on maximum equivalent bubble diameter at a mass flow rate of 1.4 g/s.

Fig. 8. Relationship between circularity and flow rate in MCHXs with different pin-fin shapes.

elongated shapes. Additionally, at low flow rates, bubbles in prismatic MCHXs exhibit slightly higher circularity than those in drop MCHXs. However, with increasing flow rate, the difference between them becomes more pronounced. In drop microchannels, enhanced shear forces at the trailing edge facilitate bubble deformation, while prismatic MCHXs, due to corner-induced complex vortices, make bubbles more prone to deformation or even rupture, ultimately resulting in the lowest circularity [30].

Fig. 9 illustrates the relationship between bubble velocity and mass flow rate in MCHXs with three pin-fin shapes. As the mass flow rate increases, bubble velocity rises correspondingly for all shapes due to the enhancement of turbulent kinetic energy within the channel. When the mass flow rate increases from 0.6 g/s to 1.4 g/s, the bubble velocities increase by 131.3 % for the circular shape, 169.5 % for the diamond shape, and 138.4 % for the drop shape. Among the three pin-fin shapes, the diamond-shaped channel exhibits the highest bubble velocity, followed by the circular and then the water drop shape. This is due to the angular features of the diamond-shaped channel, which induce stronger vortex disturbances, significantly enhancing bubble movement speed. In contrast, the streamlined boundaries of the circular and water drop-shaped channels effectively suppress flow separation. At a mass flow rate of 1.4 g/s, the bubble velocity in the diamond-shaped channel is 62.1 % higher than that in the circular channel and 78.8 % higher than that
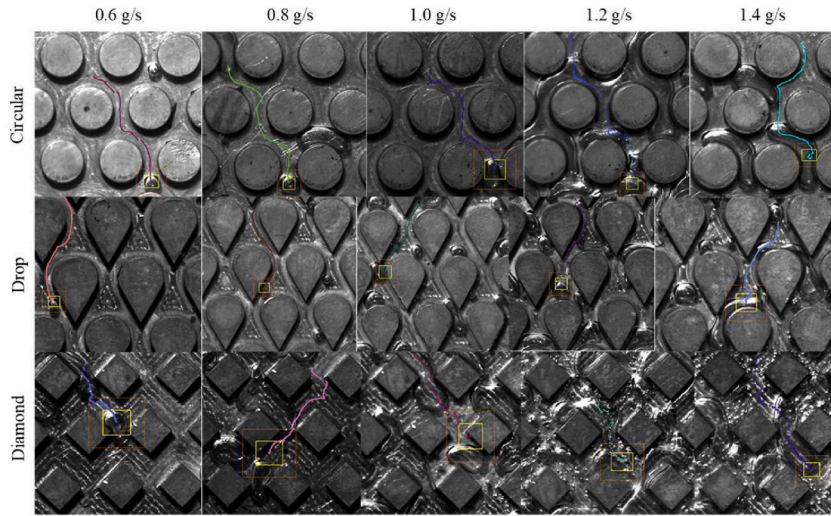
(a) Variation of bubble trajectory with mass flow rate
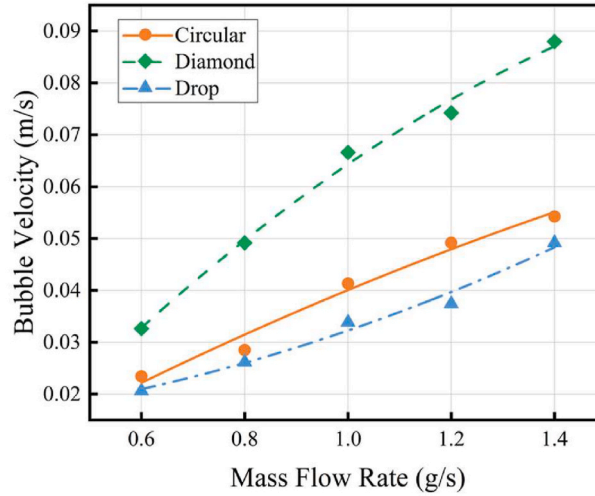
(b) Variation of bubble velocity with mass flow rate

Fig. 9. Variation of bubble trajectory with mass flow rate.

in the water drop-shaped channel.

Fig. 10 illustrates a comparison of temperature distributions at multiple positions within MCHXs of different pin-fin shapes, under a mass flow rate of 1.4 g/s and a heating power of 140 W. The average temperature in the MCHXs with circular, drop, and diamond pins are 56 °C, 61 °C, and 58 °C, respectively. Thus, the circular MCHX shows the highest two-phase heat transfer capacity, followed by drop pin, while the MCHX with diamond pin-fin array exhibits the poorest capacity. Similarly, temperature uniformity is also the highest in circular MCHXs. This is attributed to the stable flow of liquid and bubbles, which enhances heat transfer efficiency. In contrast, diamond MCHXs exhibit the lowest heat transfer capacity and temperature uniformity, primarily due to the presence of flow recirculation zones, bubble accumulation in corner regions, and non-uniform temperature distribution, leading to reduced heat transfer efficiency [31].

Fig. 11 presents the boiling curves of MCHXs with different shapes at a mass flow rate of 1.4 g/s. Overall, circular MCHXs exhibit the highest heat transfer efficiency, while diamond MCHXs exhibit the lowest. However, after exceeding the critical heat flux (CHF) and entering the initial stage of deteriorated heat transfer in film boiling, the heat transfer efficiency of all MCHXs becomes comparable. This is primarily due to the formation of a vapor film, which reduces heat transfer capabilities across all channels, causing their heat transfer performance to converge during the initial phase of deterioration [32]. As the heat flux further increases, differences in vapor film thickness, stability, and flow patterns emerge among the MCHXs, leading to divergent heat transfer performance once
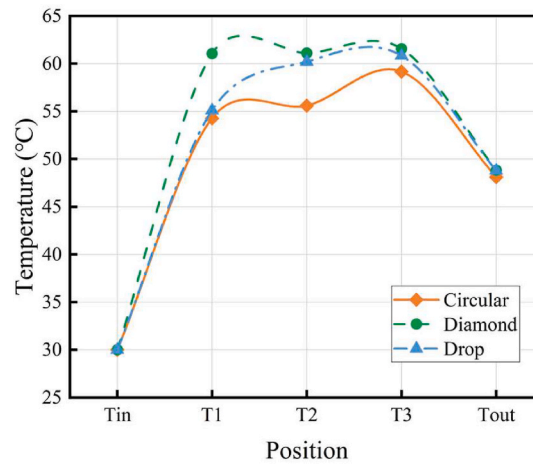
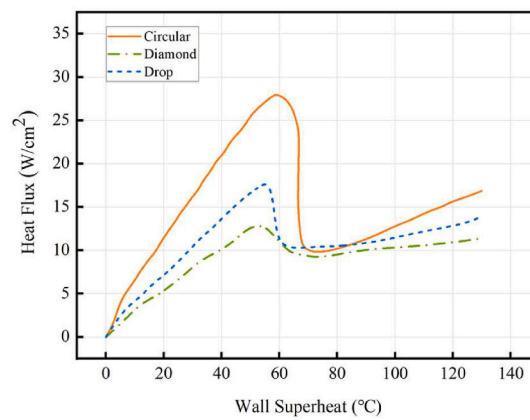**Fig. 10.** Temperature at Different Locations in MCHXs with different Shapes.

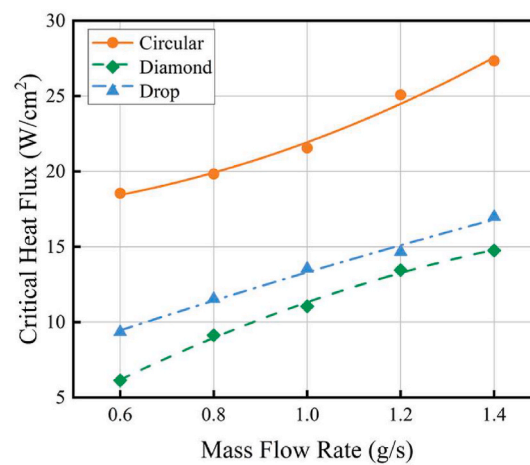**Fig. 11.** Boiling curves of MCHX with different pin-fin shapes.

Fig. 12. CHF in different pin-fin MCHX under various mass flow rates.

again. During the experiments, the critical heat fluxes for circular, diamond, and drop shapes are 27.3 W/cm^2,14.8 W/cm^2, and 16.9 W/cm^2, respectively. The points where the MCHX with three pin-fin shapes reach the critical heat flux are all close to the wall superheat of 60 °C. The shape with the poorer heat transfer effect will reach the critical point earlier.

Fig. 12 illustrates the critical heat flux (CHF) in microchannels with different shapes under various mass flow rates. The results indicate that the circular pin-fin array exhibits the highest CHF, reaching 27.3 W/cm^2, primarily due to its superior flow uniformity, enhanced wall wettability, and faster bubble detachment [33]. The drop pin-fin array ranks second, with a CHF of 16.9 W/cm^2, demonstrating relatively favourable flow characteristics. However, the increased shear force in the trailing region may lead to the premature formation of local dry spots [34]. The diamond pin-fin array exhibits the lowest CHF, only 14.8 W/cm^2, mainly due to flow non-uniformity in the corner regions, where bubble accumulation reduces heat transfer efficiency. Furthermore, in all microchannels, CHF increases with rising mass flow rates. This is primarily attributed to higher flow velocities enhancing liquid redistribution and turbulent heat transfer, effectively suppressing localized dry out phenomena.

4. Conclusions

This research comprehensively examined the heat transfer and two-phase flow behaviors within microchannel heat sinks featuring various pin-fin shapes, leading to the following key findings:

(1) Drop-shaped pin-fin array generates the smallest bubbles, while the MCHX with diamond pin-fin array form the largest bubbles due to bubble accumulation in corner regions. The maximum bubble diameters for diamond, circular, and drop are increased by 135 %, 292 %, and 601 %, respectively, with the mass flow rate increasing from 0.6 g/s to 1.4 g/s.

(2) The pressure drop rises as the mass flow rate and bubble diameter increases. Drop pin-fin arrangement exhibits the lowest flow resistance, whereas diamond microchannels experience the highest resistance. At a mass flow rate of 1.4 g/s, the pressure drop of the microchannels with diamond pin-fin is approximately 188 % higher than that of the microchannel with circular pin-fin array and about 319 % greater than the microchannel with drop pin-fin array.

(3) Microchannel with circular array demonstrate the highest heat transfer efficiency, followed by drop microchannels, while diamond microchannels perform the worst due to non-uniform temperature distribution and the presence of recirculation zones.

(4) Circular pin-fin array exhibits the highest CHF, followed by drop microchannels, while diamond microchannels have the lowest CHF. At a mass flow rate of 1.4 g/s, the circular microchannels achieved a critical heat flux of 27.3 W/cm^2, exceeding the diamond by 43.3 % and the drop by 15.1 %.

CRediT authorship contribution statement

Declaration of competing interest

The authors declare that they have no known competing financial interests or personal relationships that could have appeared to influence the work reported in this paper.

Data availability

Data will be made available on request.

References

[1] Wenlong Dong, et al., Research progress on passive enhanced heat transfer technology in microchannel heat sink, Int. J. Heat Mass Tran. 220 (2024) 125001.
[2] Zhi-Qiang Yu, Li Mo-Tong, Bing-Yang Cao, A comprehensive review on microchannel heat sinks for electronics cooling, Int. J. Extrem. Manuf. 6 (2) (2024) 022005.
[3] G. Marseglia, et al., Enhancement of microchannel heat sink heat transfer: comparison between different heat transfer enhancement strategies, Exp. Therm. Fluid Sci. 150 (2024) 111052.
[4] Guilian Wang, et al., Experimental and numerical investigation of hydrothermal performance of a microchannel heat sink with pin fins, Case Stud. Therm. Eng. 60 (2024) 104631.
[5] Jacqueline Barber, et al., Hydrodynamics and heat transfer during flow boiling instabilities in a single microchannel, Appl. Therm. Eng. 29 (7) (2009) 1299–1308.
[6] Longlong Feng, et al., Flow pattern-based heat transfer analysis of microchannel flow boiling: an experimental investigation, Case Stud. Therm. Eng. 54 (2024) 104016.
[7] Yogesh K. Prajapati, Manabendra Pathak, Kaleem Khan Mohd, A comparative study of flow boiling heat transfer in three different configurations of microchannels, Int. J. Heat Mass Tran. 85 (2015) 711–722.
[8] Neima Brauner, David Moalem Maron, Identification of the range of 'small diameters' conduits, regarding two-phase flow pattern transitions, Int. Commun. Heat Mass Tran. 19 (1) (1992) 29–39.
[9] Cheng Jin, et al., Experimental study on the flow pattern and local heat transfer characteristics of water flow boiling in a vertical upward narrow rectangular channel heated by steam, Appl. Therm. Eng. 247 (2024) 123091.
[10] Shengjie Gu, et al., Study of flow pattern transition criterion and heat transfer characteristics in vertical rectangular narrow channel for steam heating, Int. J. Heat Mass Tran. 220 (2024) 124877.
[11] Hao Yu, et al., Influence of transient heat flux on boiling flow pattern in a straight microchannel applied in concentrator photovoltaic systems, Int. J. Heat Mass Tran. 190 (2022) 122792.

[12] Hanwen Xue, et al., Experimental study on boiling flow patterns of the zeotropic mixtures of R290/R600a in a horizontal smooth tube, Int. J. Heat Mass Tran. 196 (2022) 123268.

[13] Meijuan Chang, et al., Dynamic characteristics of R1234ze (E) boiling two-phase flow patterns and heat transfer in a horizontal tube, Int. J. Heat Mass Tran. 236 (2025) 126311.

[14] Hong-Cheol Shin, et al., An experimental study on air-oil flow patterns in horizontal pipes using two synthetic oils, Int. J. Heat Mass Tran. 226 (2024) 125459.

[15] Rong Situ, et al., Photographic study of bubble behaviors in forced convection subcooled boiling, Int. J. Heat Mass Tran. 47 (17–18) (2004) 3659–3667.

[16] Burak Markal, Beyzanur Kul, Influence of downstream cross-sectional area ratio on flow boiling characteristics of expanding micro pin fin heat sinks, Int. Commun. Heat Mass Tran. 143 (2023) 106689.

[17] Guodong Wang, Ping Cheng, A.E. Bergles, Effects of inlet/outlet configurations on flow boiling instability in parallel microchannels, Int. J. Heat Mass Tran. 51 (9–10) (2008) 2267–2281.

[18] Rohit R. Bhide, et al., An active control strategy for reduction of pressure instabilities during flow boiling in a microchannel, J. Micromech. Microeng. 21 (3) (2011) 035021.

[19] R.R. Bhide, et al., Pressure drop and heat transfer characteristics of boiling water in sub-hundred micron channel, Exp. Therm. Fluid Sci. 33 (6) (2009) 963–975.

[20] Kai Fu, Xianghua Xu, Xingang Liang, An experimental study of the effects of porosity and ratio of fin to channel width on water flow boiling in copper foam fin microchannels, Int. J. Heat Mass Tran. 226 (2024) 125528.

[21] D. Sathish Kumar, S. Jayavel, Optimization of porous fin location and investigation of porosity and permeability effects on hydro-thermal behavior of rectangular microchannel heat sink, Int. Commun. Heat Mass Tran. 129 (2021) 105737.

[22] Mayur Darekar, et al., Liquid–liquid two-phase flow patterns in Y-junction microchannels, Ind. Eng. Chem. Res. 56 (42) (2017) 12215–12226.

[23] A.A. Donaldson, D.M. Kirpalani, A. Macchi, Curvature induced flow pattern transitions in serpentine mini-channels, Int. J. Multiphas. Flow 37 (5) (2011) 429–439.

[24] Subhakanta Moharana, et al., Investigation of thermal-hydraulic performance of circular, elliptical & mixed circular-elliptical tube bundles for two-phase cross-flow boiling, Int. J. Heat Mass Tran. 232 (2024) 125970.

[25] Odumuyiwa A. Odumosu, et al., Growth of elongated vapor bubbles during flow boiling heat transfer in wavy microchannels, Appl. Therm. Eng. 223 (2023) 119987.

[26] Ming Peng, et al., Numerical study on flow and heat transfer in a multi-jet microchannel heat sink, Int. J. Heat Mass Tran. 157 (2020) 119982.

[27] Xiaoyu Tang, et al., Experimental study on flow boiling heat transfer in open copper microchannel heat sinks with different aspect ratios, Int. J. Heat Mass Tran. 231 (2024) 125879.

[28] Long Zeng, et al., Thermal and flow performance in microchannel heat sink with open-ring pin fins, Int. J. Mech. Sci. 200 (2021) 106445.

[29] Mohammed W. Sulaiman, Wang Chi-Chuan, Effect of contraction on the convective boiling heat transfer of microchannel heat sinks, Appl. Therm. Eng. 223 (2023) 120026.

[30] Yuhui Pan, et al., Study on the flow and heat transfer characteristics of pin-fin manifold microchannel heat sink, Int. J. Heat Mass Tran. 183 (2022) 122052.

[31] Junhao Liu, et al., Temperature uniformity analysis and multi-objective optimization of the microchannel heat sink with cavities under longitudinal vortex flow, Int. J. Therm. Sci. 201 (2024) 109034.

[32] Xiang Ma, et al., Flow boiling instability and pressure drop characteristics based on micro-pin-finned surfaces in a microchannel heat sink, Int. J. Heat Mass Tran. 195 (2022) 123168.

[33] Chengyu Hu, et al., Research on heat transfer and flow distribution of parallel-configured microchannel heat sinks for arrayed chip heat dissipation, Appl. Therm. Eng. 255 (2024) 124003.

[34] Faraz Ahmad, et al., Effect of cross-sectional geometry on hydrothermal behavior of microchannel heat sink, J. Non-Equilibrium Thermodyn. 47 (3) (2022) 269–287.